Journal of
Applied Crystallography
ISSN 0021-8898

Blind source separation and automatic tissue typing of microdiffraction data by hierarchical nonnegative matrix factorization

Massimo Ladisa, Antonio Lamura and Teresa Laudadio

J. Appl. Cryst. (2013). **46**, 1467–1474

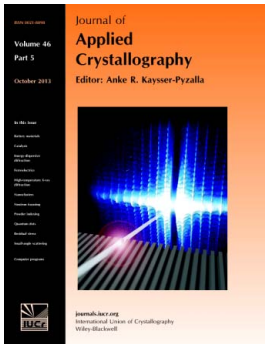

Journal of Applied Crystallography covers a wide range of crystallographic topics from the viewpoints of both techniques and theory. The journal presents papers on the application of crystallographic techniques and on the related apparatus and computer software. For many years, the *Journal of Applied Crystallography* has been the main vehicle for the publication of small-angle scattering papers and powder diffraction techniques. The journal is the primary place where crystallographic computer program information is published.

Journal of
Applied Crystallography
ISSN 0021-8898

Received 30 April 2013
Accepted 3 August 2013

Blind source separation and automatic tissue typing of microdiffraction data by hierarchical nonnegative matrix factorization

Massimo Ladisa,[a] Antonio Lamura[b]* and Teresa Laudadio[a]

[a]Istituto di Cristallografia (IC-CNR), Via G. Amendola 122/O, I-70126 Bari, Italy, and [b]Istituto per le Applicazioni del Calcolo '*Mauro Picone*' (IAC-CNR), Via G. Amendola 122/D, I-70126 Bari, Italy. Correspondence e-mail: a.lamura@ba.iac.cnr.it

In this article a nonnegative blind source separation technique, known as nonnegative matrix factorization, is applied to microdiffraction data in order to extract characteristic patterns and to determine their spatial distribution in tissue typing problems occurring in bone-tissue engineering. In contrast to other blind source separation methods, nonnegative matrix factorization only requires nonnegative constraints on the extracted sources and corresponding weights, which makes it suitable for the analysis of data occurring in a variety of applications. In particular, here nonnegative matrix factorization is hierarchically applied to two-dimensional meshes of X-ray diffraction data measured in bone samples with implanted tissue. Such data are characterized by nonnegative profiles and their analysis provides significant information about the structure of possibly new deposited bone tissue. A simulation and real data studies show that the proposed method is able to retrieve the patterns of interest and to provide a reliable and accurate segmentation of the given X-ray diffraction data.

1. Introduction

Recent studies have shown that crystallography could play a crucial role in bone-tissue engineering, whose main goal is to repair bone defects and to reconstruct highly damaged bone segments. In this context, a promising approach consists in exploiting the patient's own bone marrow stromal cells, which are isolated, expanded *in vitro*, loaded onto a bioceramic scaffold and, finally, reimplanted into the lesion site (Cedola *et al.*, 2006, 2007; Komlev *et al.*, 2006). Nowadays, *in vivo* studies are carried out by implanting small cubic scaffolds in mice for periods of a few months. In order to monitor the mechanism of new bone-tissue deposition and scaffold resorption, a great number of two-dimensional images, folded into one-dimensional X-ray diffraction (XRD) patterns, are acquired by synchrotron radiation and, afterwards, analysed.

XRD is a nondestructive technique to investigate the atomic sample structure where measured signals are real and positive. Different methods can be adopted to detect the tissues characterizing the bone sample under investigation. According to Rietveld analysis (Young, 1993; Guinier, 1994), the XRD profiles are modelled as a linear combination of known signals of pure (or combined) materials, whose coefficients (phases) provide the fractions of the corresponding materials. Although such a method accurately estimates the different phases characterizing the XRD data, it is computationally expensive and, above all, time demanding as the computational time can range between a few seconds and several weeks for a single pattern, according to the complexity of the powder structure and to the number of the parameters to be refined.

Ladisa *et al.* (2007) introduced a reliable and significantly more efficient tissue typing method, which makes use of a statistical algorithm known as canonical correlation analysis (CCA) (Johnson & Wichern, 1998; Friman, 2003; Laudadio *et al.*, 2005, 2008; De Vos *et al.*, 2006; Edelenyi *et al.*, 2000), whose application requires the knowledge of accurate model patterns that should be available *a priori* (Altamura *et al.*, 2012; Cancedda *et al.*, 2007; Guagliardi *et al.*, 2007, 2009, 2010; Giannini *et al.*, 2012).

In this paper we formulate the estimation of XRD model patterns as a blind source separation (BSS) problem. More precisely, given an XRD data set, we assume that the profile corresponding to each bone-tissue volume element (voxel) can be approximately described as a linear combination of some constituent tissue profiles. Given the nonnegative nature of the XRD data and the possible correlation that could characterize the profiles of the constituent tissues, here we propose to apply nonnegative matrix factorization (NNMF) (Paatero & Tapper, 1994; Lee & Seung, 1999), a BSS technique which only requires nonnegative constraints on the extracted sources and corresponding weights. Indeed, the lack of *a priori* information makes NNMF a suitable method to solve the problem of extracting characteristic patterns from XRD data, as it is a completely blind source separation technique. NNMF has already been applied to XRD data by Long *et al.* (2009) to analyse hundreds of XRD patterns from a combinatorial materials library.

Here, NNMF is embedded into a hierarchical scheme in order to provide model patterns to be used by other classification techniques (*e.g.* CCA). Such an approach is necessary as the signals characterizing the considered application can be highly correlated (see §4.1), while the signals considered by Long *et al.* (2009) do not present such a feature. Extensive studies performed on simulated as well as on real data show that hierarchical NNMF (HNNMF) is able to retrieve the model patterns of interest, which could be afterwards used in order to build the subspace models needed by CCA. Furthermore, the linear combination weights associated with the extracted patterns can be used to automatically segment and classify the given data set (without any quantification purpose), thereby avoiding the use of CCA to tissue type the sample. The performances of HNNMF and CCA were then compared in terms of accuracy on both simulated and real data.

The paper is organized as follows. In §2 the main crystallographic features of the measured XRD data and their acquisition environment are described. §3 is devoted to the basic principles of NNMF and to its hierarchical application to XRD data. In §4 the results of the simulation and real data studies are reported and discussed. Finally, the main conclusions are formulated.

2. Experimental

Skelite (Millenium Biologix Corporation, Kingston, Canada), a clinically available bone-graft substitute made of a mixture of silicon-stabilized tricalcium phosphate (Si-Tcp) [see Guagliardi *et al.* (2007), and references therein, for details about scaffold preparation and cell culture], hydroxyapatite (Ha) and β-tricalcium phosphate (β-Tcp), was used as bioceramic scaffold. Small cubes of $4 \times 4 \times 4$ mm were seeded with bone marrow stromal cells and implanted subcutaneously in mice for two and six months, then harvested, and suitably treated to prepare sections of about 100 µm thickness to be investigated by X-ray microdiffraction. The sections were cut so as to be transverse to the scaffold's pore surface and to preserve, as much as possible, a homogeneous composition along the thickness. All the procedures were in agreement with protocols approved by the competent ethical authority.

Measurements were carried out at beamline ID13 of the European Synchrotron Radiation Facility (ESRF). A microdiffraction setup provided with an Si 111 monochromator and a Kirkpatrick–Baez mirror system supplied a beam size of 1×1 µm with a wavelength of 0.976 Å. Patterns were recorded, in transmission mode, using a marCCD detector. A data set of NIST standard Si 640c was also collected, to be used as a standard for sample-to-detector distance determination. The investigated area of about 0.7×0.7 mm was scanned following a grid step of 25 µm.

From the two-dimensional diffraction images of the measured grid (an array of voxels of two-dimensional diffraction patterns) (Cedola *et al.*, 2007), one-dimensional patterns (one per voxel) were obtained by using the algorithm developed by Cervellino *et al.* (2005, 2006, 2008). Skelite powder, as commercially available before implant, was used to collect the diffraction pattern of the scaffold, to be used as a reference and test pattern for crystal structure models. Each diffraction pattern corresponds to the azimuthal integration of the measured signal over the sample-to-detector cylindrical symmetry (the geometry of the X-ray powder diffraction) and is represented by an intensity signal *versus* the 2θ scattering angle (representing the angle between the transferred momentum and the incoming X-ray beam) (signal of length $N = 1024$). Specifically, in our studies $2\theta \in [5^\circ, 29^\circ]$.

3. The method

The general NNMF problem is formulated as follows. Given a nonnegative matrix $X \in \Re^{n\times m}$, and a positive integer $k < \min(m, n)$, the aim is to find two nonnegative matrices $W \in \Re^{n\times k}$ and $H \in \Re^{k\times m}$ that minimize the following functional:

$$f(W, H) = \tfrac{1}{2}||X - W H||_{\rm F}^2, \qquad (1)$$

where the subscript F stands for the Frobenius norm. It is worth noticing that, given the nonconvex nature of $f(W, H)$, its minimization may lead to the estimation of local minima and may not admit a unique solution. In order to deal with such problems, several NNMF algorithms have been proposed in the literature. A significant review is reported by Berry *et al.* (2007). In particular, an interesting algorithm is proposed by Kim & Park (2007), based on an alternating nonnegativity constrained least-squares implementation, which guarantees the convergence to a stationary point.

In this paper we apply the NNMF implementation available in MATLAB (a registered trademark of The MathWorks Inc., Natick, MA, USA), which is based on an alternating least-squares (ALS) scheme (Berry *et al.*, 2007). As described in the aforementioned reference, ALS exploits the convexity properties of equation (1) in either W or H and, therefore, given one of the two matrices, the other can be found by solving a least-squares problem. In order to apply NNMF to XRD data, these are arranged into a matrix, where each row contains a profile from one voxel. Given the number of constituent profiles to be extracted, NNMF is applied to in order to obtain the nonnegative matrices that minimize equation (1). When applying NNMF for feature extraction, the matrix H is called the basis matrix and its rows contain the extracted constituent profiles, while the matrix W, known as the coefficient matrix, contains the corresponding linear combination weights, which provide information about the concentration of the obtained constituent profiles within each voxel.

The choice of the optimal value, *i.e.* the number of profiles to be extracted, represents a crucial step and is application dependent. It is up to crystallographers to state the number of possible constituent patterns that may characterize the data to be processed, *a priori*. Once k is known, NNMF is applied by following a multilevel, or hierarchical, scheme. This idea has already been introduced by Sajda *et al.* (2004) and Li *et al.* (2012) to segment and classify chemical shift imaging data and consists in progressively performing several NNMF steps.

Here, the multilevel approach is properly adapted to process XRD data.

Specifically, NNMF is applied to the data matrix X by setting $k = 2$. Two patterns are extracted along with their linear combination weights. The weight vectors are reshaped, according to the XRD image dimensions, in order to show the spatial contribution of the extracted sources in each voxel. By comparing the two sets of contributions, voxel by voxel, a first rough segmentation of the given data set is obtained by assigning each voxel to the pattern characterized by the maximum weight in that voxel. Such a segmentation procedure is similar to that applied by Laudadio *et al.* (2005) to obtain nosologic images by CCA. Afterwards, NNMF is applied to each of the two subregions obtained in the previous step, by setting $k = 2$ again. Four patterns are then obtained and the corresponding weights allow the segmentation of the given XRD image into four tissue regions. If we denote the total number of patterns to be extracted by K, and the number of extracted sources at each step of the multilevel scheme by 2^{NS}, where NS represents the number of steps that have been performed, the total number of actually extracted patterns is given by the first power of 2 larger than K, here denoted by $2^{FinalNS}$. Of course, a problem arises when $2^{FinalNS} \neq K$. In such a situation, it is up to the crystallographer to decide either to keep all the extracted $2^{FinalNS}$ sources or to prune the K most interesting and informative ones for the specific application under investigation.

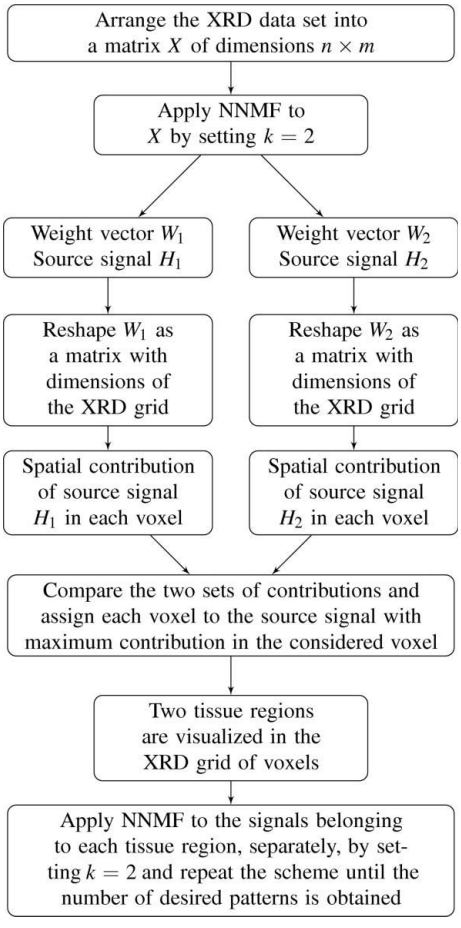

Figure 1
Scheme of the method proposed in §3.

Table 1
Weight percentages used to produce the simulated microdiffraction XRD signals displayed in Fig. 2.

Signal	Amorphous	Ha-nano	Ha-micro	Si-Tcp	β-Tcp
1	32.0	30.2	13	21.5	3.3
2	12.4	87.6	0	0	0
3	100	0	0	0	0
4	16.8	73.0	6.6	2.0	1.6
5	36.3	63.7	0	0	0
6	85.8	14.2	0	0	0

As shown by the tests carried out on simulated examples, the multilevel scheme is able to provide the model patterns of interest and an accurate segmentation and classification of the given data. Furthermore, it is more reliable than the one-shot approach, where only one step of NNMF is performed by directly setting $k = K$. Indeed, our tests show that the multilevel scheme prevents convergence problems and non-optimal NNMF solutions, which may occur when the actual rank of the matrix X is smaller than K. The structure of the proposed method is sketched in Fig. 1. The comparison between the one-shot approach and the multilevel one is analysed and described in §4.

4. Application

4.1. Simulation studies

Fig. 2 shows six characteristic microdiffraction XRD signals, sampled at a higher resolution step of 1 µm from *in vivo* data measured in the experimental setup described in §2. They represent a mixture of four crystalline phases (Ha-nano, Ha-micro, Si-Tcp, β-Tcp) and the sample bulk (amorphous) according to the weight percentages as reported in Table 1.

The above signals were exploited in order to produce a simulated XRD image, consisting of a 27×27 grid of voxels containing one-dimensional XRD signals, in which six different and well localized tissue regions, denoted by different grey levels, can be observed (see Fig. 3). The type of tissue inserted in each region is identified by the background grey level characterizing the corresponding intensity signal in Fig. 2. In order to simulate a realistic XRD data set, Poisson noise (proportional to the square root of the signal amplitude) was added to the one-dimensional patterns contained in the simulated grid. The data set was properly reshaped, and NNMF was then applied in order to extract the six constituent tissue profiles and to build the corresponding nosologic image. As described in §3, NNMF requires the data set as well as the number K of sources to be extracted as input data. Our tests showed that, if NNMF was run by setting $K = 6$ directly, convergence problems occurred as the rank of the matrix to be processed was lower than K. Such problems were highlighted by a warning message provided by MATLAB, which pointed

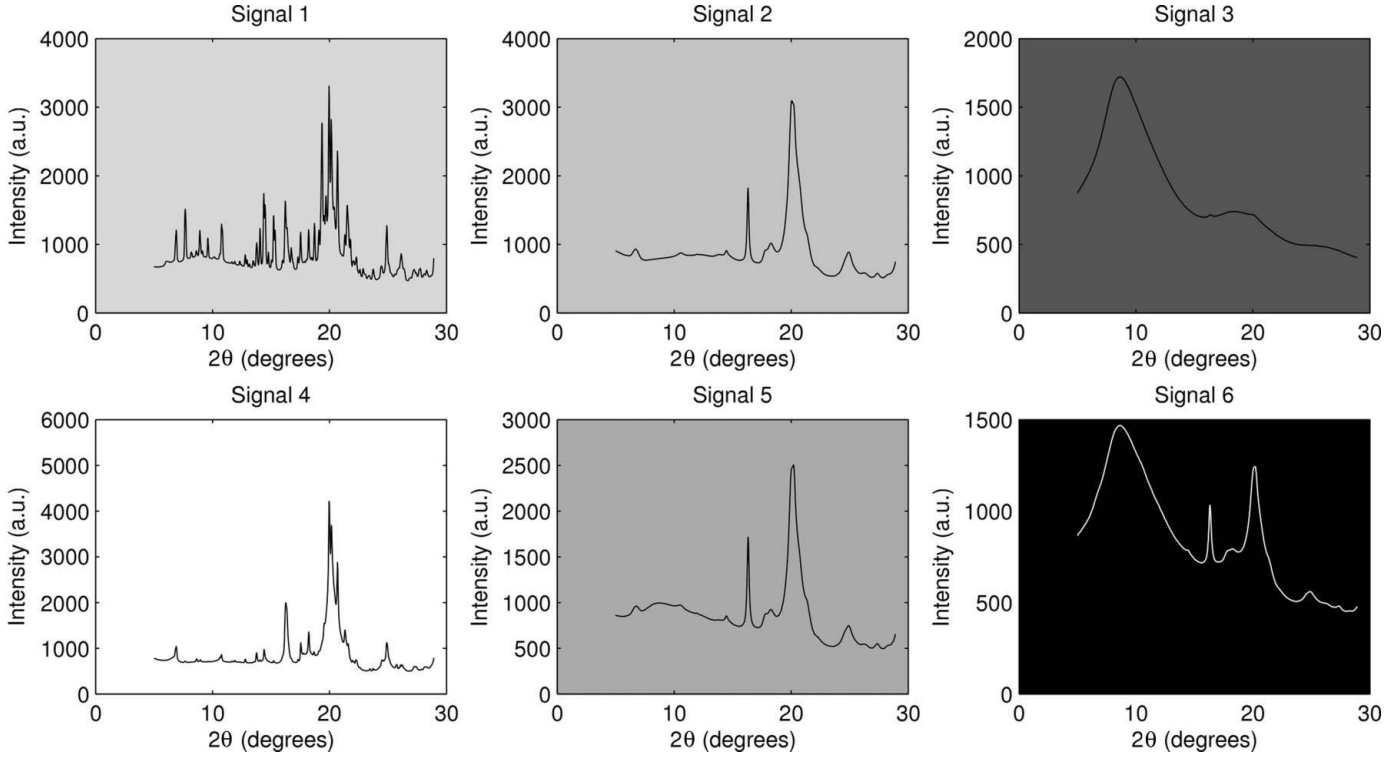

Figure 2
Characteristic microdiffraction XRD signals of length $N = 1024$ considered in the simulation studies. They represent a mixture of four crystalline phases (Ha-nano, Ha-micro, Si-Tcp, β-Tcp) and the sample bulk (amorphous) according to the weight percentages as reported in Table 1.

out that the algorithm converged to solutions of lower rank than K and, therefore, the result might be not optimal.

In order to overcome such problems, the hierarchical approach described in the previous section was applied by performing NS steps with $k = 2$ at each step. Given the number of constituent profiles to be extracted, *i.e.* $K = 6$, the natural choice for the parameter NS should be 3, thereby yielding eight extracted signals among which the six patterns of interest have to be selected. Nevertheless, we observed that some of the eight profiles extracted by HNNMF were zero signals and, therefore, one more step of HNNMF with $k = 2$ was needed in order to get six nonzero patterns. More precisely, by setting NS = 4, HNNMF provided six nonzero signals and ten zero signals. Once the algorithm has recovered the six simulated signals, increasing the number of steps only produces zero signals. Fig. 4 shows the six constituent patterns extracted by HNNMF. Below each pattern a flat line is displayed, representing the difference between the actual simulated signal reported in Fig. 2 after normalization and the corresponding one provided by HNNMF. The difference between the two types of signals is clearly negligible: HNNMF is able to accurately recover the signals characterizing the given simulated XRD image.

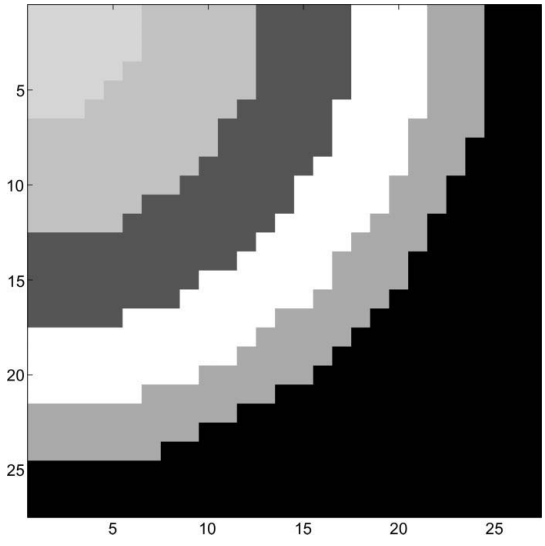

Figure 3
Simulated XRD image made of 27 × 27 voxels, where six tissue regions, denoted by different grey levels, are considered. The type of tissue in each region can be identified by matching the region grey level to the signal background depicted in Fig. 2.

The sources extracted by HNNMF can be afterwards adopted as model patterns in tissue typing methods such as CCA, which provide the spatial distribution of the different bone tissues associated with the considered model patterns within the XRD image. Fig. 5 shows the nosologic image obtained by applying CCA to the simulated XRD image in Fig. 3 when considering as model patterns, used to build the Taylor subspace models, the sources provided by HNNMF and as spatial model the symmetric 3 × 3 model without corner voxels [for details on the application of CCA to XRD data see Ladisa *et al.* (2007), and references therein]. By comparing Figs. 3 and 5, it is possible to observe that CCA is able to well

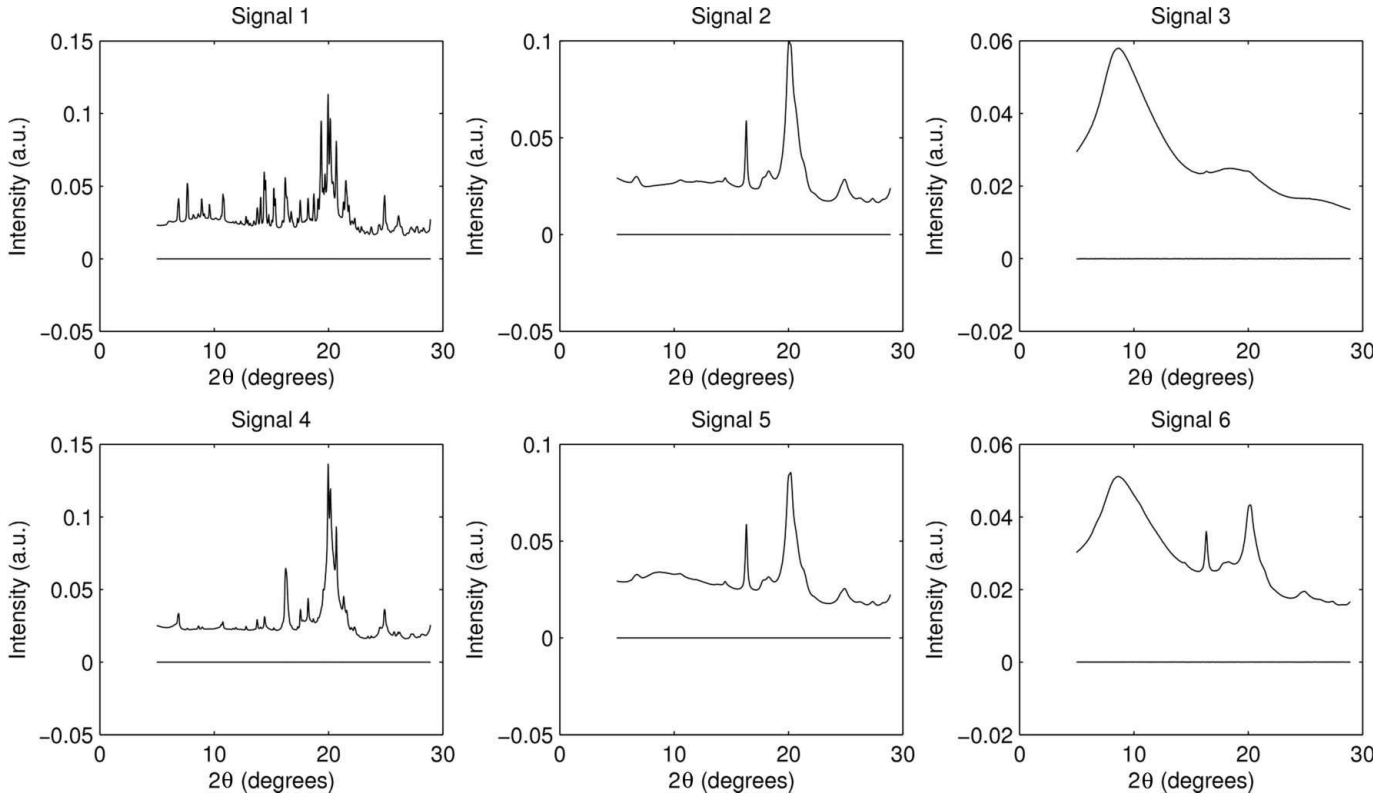

Figure 4
Source signals extracted by applying the hierarchical scheme based on NNMF to the simulated XRD image (top) and the difference with respect to the corresponding normalized signals of Fig. 2 (bottom). HNNMF is able to accurately recover the signals characterizing the given simulated XRD image, as the difference between the two types of signals is clearly negligible.

localize the six different tissue regions, although some border voxels are misclassified between region 1 and region 2, and between regions 3 and 4. Such behaviour can be explained by the significant difference in shape of the signals in the above-mentioned contiguous regions. Indeed, as described by Ladisa *et al.* (2007), when classifying a voxel, CCA exploits information contained in that voxel as well as in the neighbouring

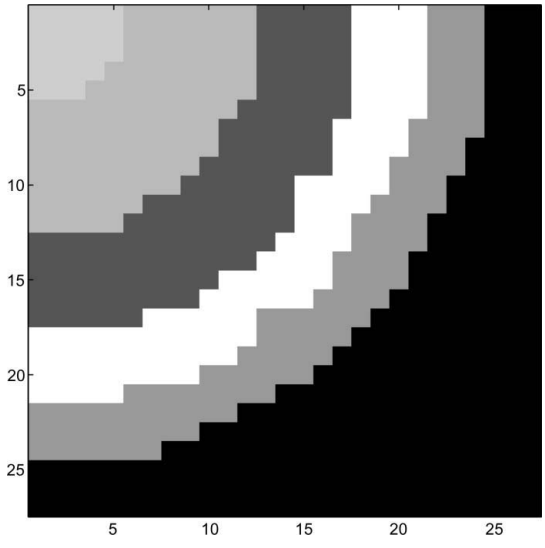

Figure 5
Nosologic image, made of 27 × 27 voxels, obtained by applying CCA to the simulated XRD image by using as model patterns (to build the Taylor subspace models) the signals extracted by HNNMF. The type of tissue in each region can be identified by matching the region grey level to the signal background depicted in Fig. 2.

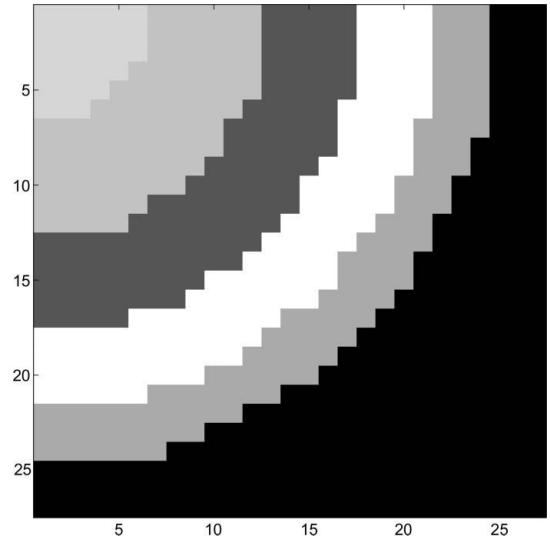

Figure 6
Nosologic image, made of 27 × 27 voxels, obtained by exploiting the weight vectors computed by HNNMF for the simulated XRD image. The type of tissue in each region can be identified by matching the region grey level to the signal background depicted in Fig. 2.

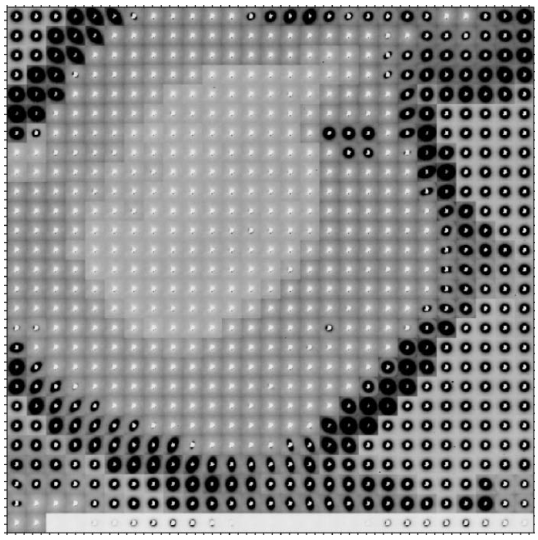

Figure 7
Screenshot of the X-ray diffraction patterns investigated in the *in vivo* studies.

ones. If contiguous signals are quite different in both peak location and shape, exploiting spatial information could sometimes be disadvantageous, even when adopting other spatial models. In that case, an additional strategy should be applied in order to correctly reclassify the border voxels.

Here, we propose an alternative and automatic tissue typing approach, which makes use of the weight vectors associated with the extracted sources by HNNMF. By following the same procedure as reported by Ladisa *et al.* (2007) to produce nosologic images, at each step of the multilevel HNNMF algorithm, a segmentation and classification of the given data set is obtained by assigning each voxel to the pattern characterized by the maximum weight in that voxel. The nosologic image obtained by HNNMF is displayed in Fig. 6 and it shows a perfect segmentation and classification, even in those voxels where CCA fails. A similar behaviour was observed by adding different noise levels to the data and by adopting other geometrical configurations of the tissue distribution within the grid.

4.2. *In vivo* studies

Fig. 7 shows the screenshot of an *in vivo* XRD image displaying the spatial variation of different structural features, thus allowing one to map the mineralization intensity and bone orientation degree around the scaffold pore. Details about the experimental setup and acquisition procedure are described in §2. HNNMF was applied in order to extract the most significant constituent patterns and to segment and classify the given data set. Concerning the choice of the K parameter, *i.e.* the number of sources to be extracted, the crystallographers who provided the data and knew the specific properties of the sample under investigation suggested to set $K = 8$. Therefore, HNNMF was applied with NS = 3. Fig. 8 shows the extracted model patterns. By a visual inspection of the profiles provided by the algorithm, it is possible to associate them with the signals of Fig. 4, keeping in mind that differences in peak heights are related to different levels of mineralization.

As in the simulated example, a nosologic image was built by exploiting the weight vectors associated with the extracted sources (see Fig. 9). Furthermore, the extracted model

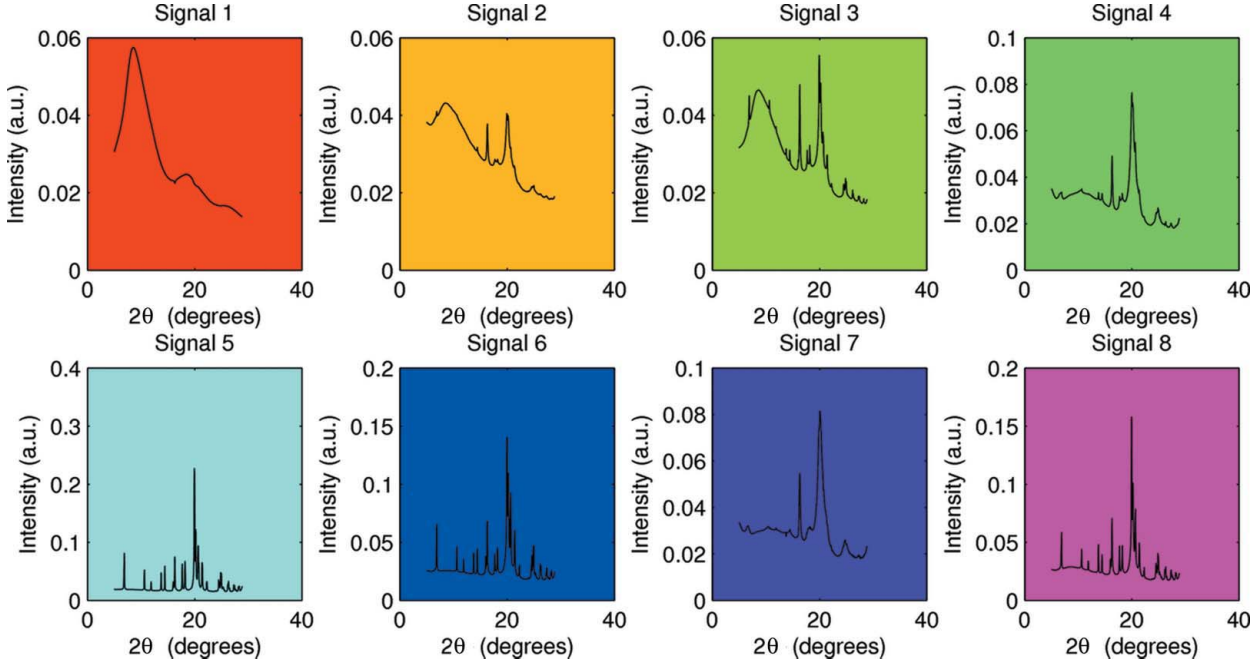

Figure 8
Source signals extracted by HNNMF when applied to the *in vivo* XRD image displayed in Fig. 7. The extracted profiles can be associated with the signals displayed in Fig. 4 and differences in peak heights point out different levels of mineralization.

patterns were used in order to build the subspace models needed by CCA. The nosologic image obtained by CCA is displayed in Fig. 10. Figs. 9 and 10 clearly show significant differences, especially in detecting the middle region associated with Signal 3 of Fig. 8, signalling the engineered pore scaffold remineralization, which is absent in Fig. 10. Moreover, the two tissue typing algorithms show different classification results in the edge region of the grid. In order to quantify the performance of the considered methods, the mean of the correlation coefficients, between the signals contained in the detected voxels for each tissue region and the corresponding ones in the *in vivo* grid, was computed for both methods. Such values are reported in Table 2. It transpires that HNNMF outperforms CCA, except for the tissue region corresponding to Signal 2 which is restricted to a few voxels, in terms of segmentation and classification.

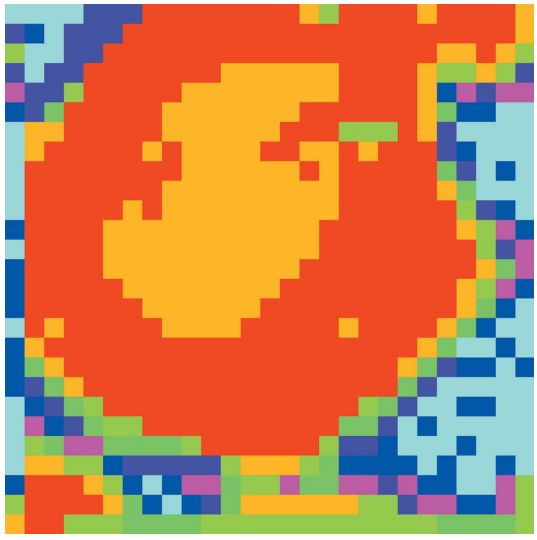

Figure 9
Nosologic image, made of 27 × 27 voxels, obtained by exploiting the weight vectors computed by HNNMF for the *in vivo* XRD image. Colours correspond to those depicting the signal background in Fig. 8. HNNMF is able to detect a middle region associated with Signal 3 of Fig. 8, indicating the engineered pore scaffold remineralization, which is undetected by CCA (see Fig. 10).

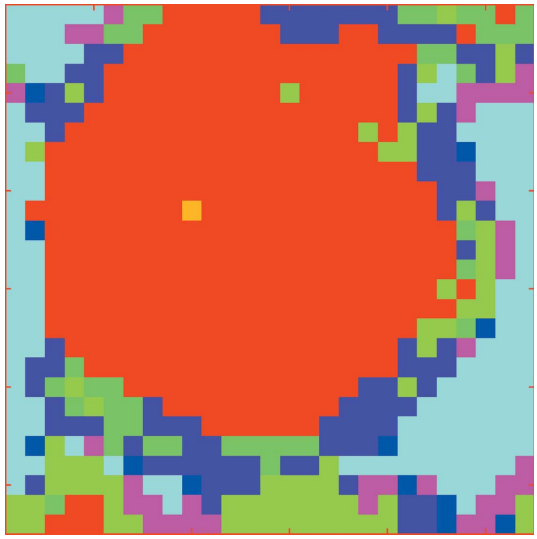

Figure 10
Nosologic image, made of 27 × 27 voxels, obtained by applying CCA to the *in vivo* XRD image by using as model patterns (to build the Taylor subspace models) the signals extracted by HNNMF. Colours correspond to those depicting the signal background in Fig. 8.

Table 2
Mean of the correlation coefficients between the signals contained in the detected voxels for each tissue region and the corresponding ones in the *in vivo* grid of Fig. 7.

Region corresponding to	HNNMF	CCA
Signal 1	0.9972	0.9847
Signal 2	0.9477	0.9700
Signal 3	0.9354	0.9165
Signal 4	0.8779	0.5915
Signal 5	0.9627	0.8584
Signal 6	0.9492	0.8267
Signal 7	0.9690	0.5981
Signal 8	0.9485	0.8837

5. Conclusions

In this paper we have proposed a method for tissue typing of XRD data acquired from a clinically available scaffold implanted in a damaged bone. The technique is based on HNNMF (*i.e.* NNMF embedded into a hierarchical scheme) and is able to provide reliable tissue segmentation and classification of the sample by its direct visualization. Extensive simulation and *in vivo* studies show that HNNMF accounts for a systematic analysis of the materials as they appear in the X-ray diffraction patterns. Furthermore, the performed analysis shows that HNNMF outperforms CCA, making it a promising numerical tool to investigate new applications such as, for instance, the mineralization orientation.

The authors would like to thank C. Giannini and D. Siliqi of Istituto di Cristallografia (IC), Consiglio Nazionale delle Ricerche, Bari (Italy), for kindly providing the experimental crystallographic data. Moreover, they would like to thank Dr Diana M. Sima and Yuqian Li of the Electrical Engineering Department, Katholieke Universiteit Leuven, Leuven (Belgium), for fruitful discussions on theoretical and applicative aspects of NNMF.

References

Altamura, D., Lassandro, R., Vittoria, F. A., De Caro, L., Siliqi, D., Ladisa, M. & Giannini, C. (2012). *J. Appl. Cryst.* **45**, 869–873.
Berry, M. W., Browne, M., Langville, A. N., Pauca, V. P. & Plemmons, R. J. (2007). *Comput. Stat. Data Anal.* **52**, 155–173.
Cancedda, R., Cedola, A., Giuliani, A., Komlev, V., Lagomarsino, S., Mastrogiacomo, M., Peyrin, F. & Rustichelli, F. (2007). *Biomaterials*, **28**, 2505–2524.
Cedola, A., Mastrogiacomo, M., Burghammer, M., Komlev, V., Giannoni, P., Cancedda, R., Rustichelli, F., Favia, A. & Lagomarsino, S. (2006). *Phys. Med. Biol.* **51**, 109–116.
Cedola, A., Mastrogiacomo, M., Lagomarsino, S., Cancedda, R., Giannini, C., Guagliardi, A., Ladisa, M., Burghammer, M.,

Rustichelli, F. & Komlev, V. (2007). *Spectrochim. Acta B*, **62**, 642–647.
Cervellino, A., Giannini, C., Guagliardi, A. & Ladisa, M. (2005). *J. Appl. Cryst.* **38**, 685–687.
Cervellino, A., Giannini, C., Guagliardi, A. & Ladisa, M. (2006). *J. Appl. Cryst.* **39**, 745–748.
Cervellino, A., Giannini, C., Guagliardi, A. & Ladisa, M. (2008). *J. Appl. Cryst.* **41**, 701–704.
De Edelenyi, F. S., Rubin, C., Estève, F., Grand, S., Décorps, M., Lefournier, V., Le Bas, J. F. & Rémy, C. (2000). *Nat. Med.* **6**, 1287–1289.
De Vos, M., Laudadio, T., Simonetti, A. W., Heerschap, A. & Van Huffel, S. (2006). *J. Magn. Reson.* **184**, 292–301.
Friman, O. (2003). PhD thesis, Department of Biomedical Engineering, Linköpings University, Sweden.
Giannini, C., Siliqi, D., Bunk, O., Beraudi, A., Ladisa, M., Altamura, D., Stea, S. & Baruffaldi, F. (2012). *Sci. Rep.* **2**, 435.
Guagliardi, A., Cedola, A., Giannini, C., Ladisa, M., Cervellino, A., Sorrentino, A., Lagomarsino, S., Cancedda, R. & Mastrogiacomo, M. (2010). *Biomaterials*, **31**, 8289–8298.
Guagliardi, A., Giannini, C., Cedola, A., Mastrogiacomo, M., Ladisa, M. & Cancedda, R. (2009). *Tissue Eng. Part B Rev.* **15**, 423–442.
Guagliardi, A., Giannini, C., Ladisa, M., Lamura, A., Laudadio, T., Cedola, A., Lagomarsino, S. & Cancedda, R. (2007). *J. Appl. Cryst.* **40**, 865–873.
Guinier, A. (1994). *Diffraction in Crystals, Imperfect Crystals, and Amorphous Bodies*. New York: Dover.
Johnson, R. A. & Wichern, D. W. (1998). *Applied Multivariate Statistical Analysis*, 4th ed. New Jersey: Prentice Hall.
Kim, H. & Park, H. (2007). *Bioinformatics*, **23**, 1495–1502.
Komlev, V. S., Peyrin, F., Mastrogiacomo, M., Cedola, A., Papadimitropoulos, A., Rustichelli, F. & Cancedda, R. (2006). *Tissue Eng.* **12**, 3449–3458.
Ladisa, M., Lamura, A. & Laudadio, T. (2007). *EURASIP J. Adv. Signal Process.* doi: 10.1155/2007/19260.
Laudadio, T., Martínez-Bisbal, M. C., Celda, B. & Van Huffel, S. (2008). *NMR Biomed.* **21**, 311–321.
Laudadio, T., Pels, P., De Lathauwer, L., Van Hecke, P. & Van Huffel, S. (2005). *Magn. Reson. Med.* **54**, 1519–1529.
Lee, D. D. & Seung, H. S. (1999). *Nature*, **401**, 788–791.
Li, Y., Sima, D., Van Cauter, S., Himmelreich, U., Pi, Y. & Van Huffel, S. (2012). Proceedings of the International Conference on Bio-inspired Systems and Signal Processing (BIOSIGNALS 2012), Vilamoura, Portugal, Lirias No. 324706.
Long, C. J., Bunker, D., Li, X., Karen, V. L. & Takeuchi, I. (2009). *Rev. Sci. Instrum.* **80**, 103902.
Paatero, P. & Tapper, U. (1994). *Environmetrics*, **5**, 111–126.
Sajda, P., Du, S., Brown, T. R., Stoyanova, R., Shungu, D. C., Mao, X. & Parra, L. C. (2004). *IEEE Trans. Med. Imaging*, **23**, 1453–1465.
Young, R. A. (1993). *The Rietveld Method*, reprint ed. New York: Oxford University Press.